NANO LETTERS

Letter

pubs.acs.org/NanoLett

High Pressure Vibrational Properties of WS_2 Nanotubes

K. R. O'Neal,[†] J. G. Cherian,[†] A. Zak,[‡] R. Tenne,[¶] Z. Liu,[§] and J. L. Musfeldt*[,†]

[†]Department of Chemistry, University of Tennessee, Knoxville, Tennessee 37996, United States

[‡]Faculty of Sciences, Holon Institute of Technology, Holon 58102, Israel

[¶]Department of Materials and Interfaces, Weizmann Institute, Rehovot 76100, Israel

[§]Geophysical Laboratory, Carnegie Institution of Washington, Washington D.C. 20015, United States

ABSTRACT: We bring together synchrotron-based infrared and Raman spectroscopies, diamond anvil cell techniques, and an analysis of frequency shifts and lattice dynamics to unveil the vibrational properties of multiwall WS_2 nanotubes under compression. While most of the vibrational modes display similar hardening trends, the Raman-active A_{1g} breathing mode is almost twice as responsive, suggesting that the nanotube breakdown pathway under strain proceeds through this displacement. At the same time, the previously unexplored high pressure infrared response provides unexpected insight into the electronic properties of the multiwall WS_2 tubes. The development of the localized absorption is fit to a percolation model, indicating that the nanotubes display a modest macroscopic conductivity due to hopping from tube to tube.

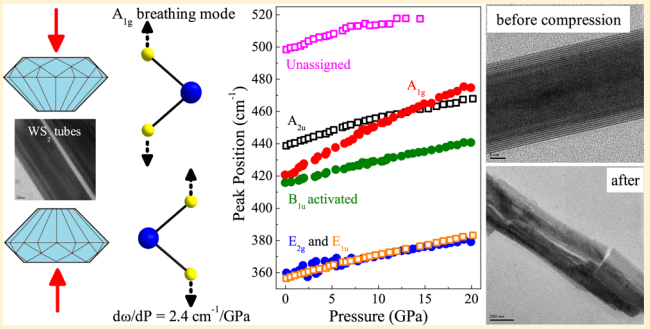

KEYWORDS: *WS_2 nanotubes, nanoscale transition metal dichalcogenides, high pressure vibrational spectroscopies, percolation*

Transition metal dichalcogenides are attracting tremendous interest due to their exotic properties and demonstrated applications.[1−6] These van der Waals solids form multiwall nanotubes (Figure 1) and nanoparticles,[7] and just like graphite, they can be cleaved into single- and few-layer sheets.[8] The tubes and particles are well-known to display superior mechanical stability[9] and solid-state lubrication properties[10−12] that have led to their commercial availability and wide use in power generation, heavy industry, and mining, and potential application in jet engines and medical devices.[13−16] Nanotube-reinforced polymer composites also benefit from the small tube size, modulus, and high aspect ratio,[17−19] as well as excellent dispersion and adhesion to the polymer matrix.[20] Under high shearing rates, however, the tubes and particles begin to deform and exfoliate.[15,21] Previous theoretical and experimental studies give some insight into the lubrication and breakdown mechanisms. For instance, modeling of the nanotubes under uniaxial pressure predicts a distortion of the tubes with the innermost layer being the most strongly affected.[22] This causes a crack to propagate from a pinching point of the innermost layer outward, resulting in two-dimensional sheets.[22] Shockwave experiments predict a similar mechanism in nanoparticles, except with the fracture originating in the outermost layer.[23] At the same time, low temperature specific heat measurements show that long wavelength acoustic modes are blocked in these confined systems.[24] This makes the high pressure vibrational properties of transition metal dichalcogenide nanotubes of great fundamental and practical importance.

The recent availability of macroscopic quantities of multiwall WS_2 nanotubes[25] provides an opportunity to reveal the behavior of different local lattice distortions under pressure and by doing so test various breakdown pathways. What differentiates our work from prior efforts[26] is that (i) we measure the infrared spectra, and (ii) the Raman response under pressure is extended from 10 GPa up to 20 GPa. Bringing together synchrotron-based infrared and Raman spectroscopies provides a comprehensive view of the different types of lattice motion, and at the same time, the larger pressure range unveils the distinguishing characteristics of each feature under compression. Comparison reveals that the A_{1g} vibration is twice as pressure sensitive as the other features. The superior hardening of this breathing mode indicates that most of the volume reduction takes place between the layers. This makes the displacement a strong candidate for driving the nanotube breakdown pathway under high strain. In fact, transmission electron microscope images after compression confirm that cracks form in the direction of the A_{1g} displacement. These findings are important for understanding (and potentially blocking) mechanical breakdown pathways in transition metal dichalcogenide nanostructures. At the same time, the electronic properties of the transition metal dichalcogenides are of fundamental and practical importance,[6,27−38] with predictions of band gap closure under pressure to be tested.[39] For example, the pressure-induced

Received: October 1, 2015
Revised: December 7, 2015
Published: December 16, 2015

DOI: 10.1021/acs.nanolett.5b03996
Nano Lett. 2016, 16, 993−999

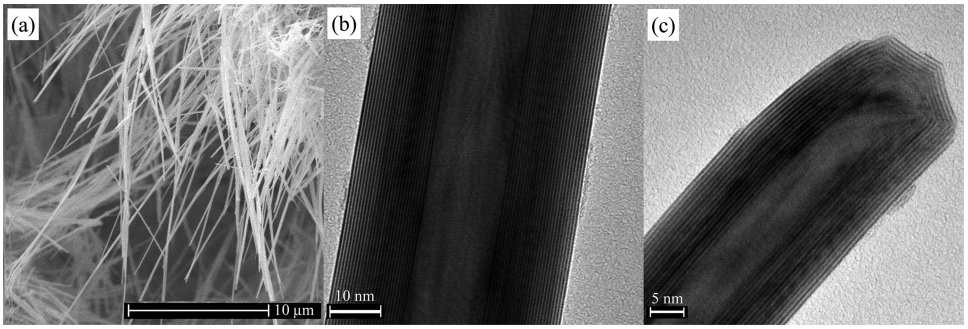

Figure 1. Ambient condition (a) scanning and (b,c) high-resolution transmission electron microscopy images of the WS_2 nanotubes used in this work.

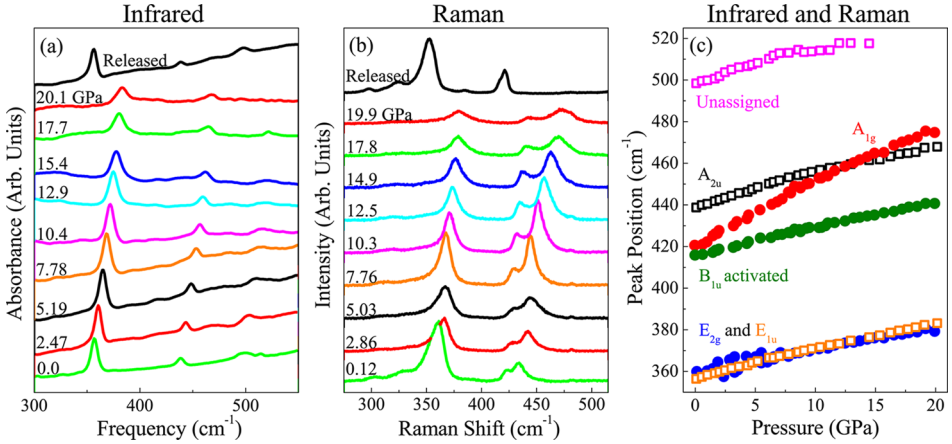

Figure 2. (a) Infrared and (b) Raman spectra of WS_2 nanotubes at the indicated pressures focusing on the observed vibrational modes. The number and position of modes are consistent with expectations, and the released spectra are taken after the compression cycle. (c) Frequency vs pressure for the infrared- (open squares) and Raman-active (closed circles) modes, displaying the stronger pressure sensitivity of the A_{1g} mode. The unassigned feature is likely a combination mode rather than a fundamental.

metallization around 19 GPa due to collapse of the interlayer spacing is already under study in bulk and multilayer MoS_2.[40−42] Bulk WS_2 is, by contrast, significantly more stable and does not show distortions or metallization up to 52 GPa.[43] The electronic properties of the WS_2 nanotubes in this work are different yet again, with the development of a localized absorption under pressure that points to modest conductivity above the percolation limit.

Vibrational Assignments and Pressure Trends. Figure 2a,b displays the infrared and Raman response of the WS_2 nanotubes. At ambient conditions, the infrared spectrum exhibits vibrational modes at 356.7, 438.3, and 498.6 cm^{-1}, which are assigned as E_{1u} symmetry, A_{2u} symmetry, and a combination mode, respectively.[44,45] The ambient pressure Raman spectrum shows features at 360.0, 415.9, and 420.7 cm^{-1}, which are assigned as E_{2g}, B_{1u}, and A_{1g} symmetry modes, respectively.[26,44,46] The latter are in excellent agreement with previous Raman measurements.[26] The displacement patterns for these modes are summarized in Figure 3, where the single crystal displacements are used in approximation of the multiwalled nanotubes. While these are all intralayer modes,[26,28,44−46] i.e., not the rigid layer modes observed at lower frequencies,[47−51] the A and B symmetry modes can still reveal interlayer interactions as their displacements have out-of-plane components. These assignments and symmetries are brought together in Table 1.

In order to better understand the microscopic aspects of tube breakdown, we investigated the vibrational properties of the WS_2 nanotubes under compression. Tracking the mode frequencies versus pressure shows that all peaks harden systematically up to 20 GPa, in line with the lack of a structural phase transition in the single crystal.[53] Bringing the peak position versus pressure data together in Figure 2(c) highlights a far more exciting trend. While the majority of features display similar hardening (with $d\omega/dP$ between 1 and 1.4 cm^{-1}/GPa),[54] the 420.7 cm^{-1} Raman mode is different, with $d\omega/dP$ on the order of 2.8 cm^{-1}/GPa (Figure 2c and Table 1). It is worth noting that while the pressure-induced frequency shift of the A_{1g} mode (and in fact all of the Raman-active modes in the WS_2 tubes) is in perfect agreement with the work of Staiger et al.[26] up to 10 GPa, the extension of our study up to 20 GPa and the ability to compare with infrared unambiguously reveals the uniqueness of the A_{1g} displacement. As we shall argue below, the large $d\omega/dP$ of the Raman-active A_{1g} mode suggests that it may be an integral part of the tube breakdown pathway. The idea that long wavelength acoustic modes are blocked in confined systems like WS_2 nanoparticles is consistent with this interpretation.[24]

To quantify these effects, we calculated the mode Grüneisen parameters as $\gamma_i = -(\partial \ln \omega_i/\partial \ln V) = (\omega_i\chi_T)^{-1}(\partial\omega_i/\partial P)$, where ω_i is the frequency of the ith mode, and $\chi_T = -V^{-1}(\partial V/\partial P)$ is the isothermal compressibility, V is the volume, and P is pressure.[43,55] As a reminder, the γ_i characterize mode stiffness. Due to the strong polarization of the vibrational modes, we also calculate a "directional Grüneisen parameter" using the unit cell parameter pertinent to the displacement in place of the cell

DOI: 10.1021/acs.nanolett.5b03996
Nano Lett. 2016, 16, 993−999

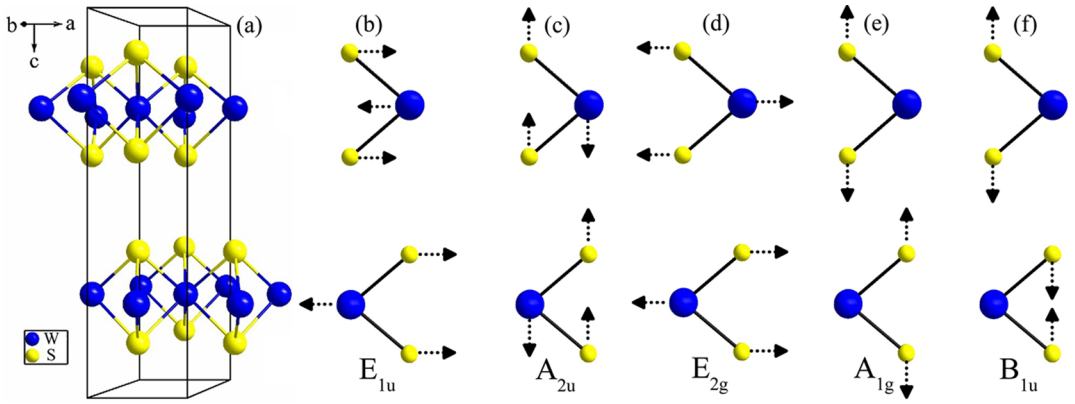

Figure 3. (a) The unit cell of WS_2 consists of two layers; in each layer W is covalently bonded to six S atoms in trigonal prismatic coordination,[52] which form the walls of the tubes. These layers comprise the *ab*-plane, and are stacked along the *c* axis. Displacement patterns for the (b,c) infrared- and (d–f) Raman-active phonons.[44,45] While these mode patterns and symmetries formally apply only to the single crystal, they are regularly extended to describe nanoscale analogues.

Table 1. Assignments, Pressure-Induced Hardening, Mode Grüneisen Parameters, and Fractional Frequency Increase for the Vibrational Modes of WS_2 Nanotubes

$\omega_{Ambient}$ (cm^{-1})	activity	symmetry	$d\omega/dP$ (cm^{-1}/GPa)	Grüneisen parameter[a]	Grüneisen parameter[b]	$(1/\omega)(d\omega/dP)$ 10^{-2} GPa^{-1}
356.7	infrared	E_{1u}	1.31 ± 0.02	0.28	0.70	0.37
438.3	infrared	A_{2u}	1.44 ± 0.03	0.25	1.67	0.33
498.6	infrared	-	1.44 ± 0.08	-	-	0.27
360.0	Raman	E_{2g}	1.05 ± 0.05	0.21	0.51	0.27
415.9	Raman	B_{1u}	1.25 ± 0.03	0.23	1.51	0.30
420.7	Raman	A_{1g}	2.79 ± 0.04	0.49	3.25	0.64

[a]Traditional Grüneisen parameters calculated using the unit cell volume. [b]"Directional" Grüneisen parameters calculated using the pressure dependence of the unit cell parameter *a* or *c* based on the displacement.[43]

volume.[43] This is done by replacing the volume derivative in the χ_T expression with that along the specific axis of interest, for instance $\chi_T = -c^{-1}(\partial c/\partial P)$ for modes with displacements along the *c* axis. We also calculated the fractional frequency increase $(1/\omega)(d\omega/dP)$ for each mode, which are in good agreement with the intralayer modes of similar layered sulfides.[50] Moreover, as an approximation, the force constant increase at 20 GPa for each mode can be estimated as $(\omega_{0GPa}/\omega_{20GPa})^2$. The A_{1g} mode force constant increased by ≈1.27, whereas the next highest increase is ≈1.15 for the E_{1u} mode. In all cases, we again see that the A_{1g} mode is unique, with values that are significantly higher than those for the other modes irrespective of the calculation method (Table 1). We conclude that the A_{1g} mode is much stiffer than the others. Similar findings are anticipated for the transition metal dichalcogenide nanoparticles.[28]

Bringing our spectroscopic findings together with an analysis of the displacement patterns reveals why the 420.7 cm^{-1} Raman mode in the WS_2 nanotubes is so sensitive to applied pressure. It is well known that interlayer van der Waals forces are weaker than the intralayer covalent bonding in transition metal dichalcogenides.[1,50] Local lattice distortions in this direction thus provide a "path of least resistance" for volume reduction. Based on this simple idea, the A and B symmetry modes are expected to show the greatest pressure dependence since they contain out-of-layer displacements. Let us consider the A_{1g} mode in this context. The displacement pattern involves in-phase out-of-plane expansion of the layers, so it is logical that it is the most affected by compression since the layers have less and less room to expand. This accounts for the magnitude of the volume and linear Grüneisen parameters in Table 1. The A_{2u} and B_{1u} modes are different, even though they also probe the elastic properties in the *c* direction. Their pressure dependencies are, in fact, similar to the E symmetry modes, a finding that can again be explained by the displacement patterns. The A_{2u} mode consists of WS_2 units counter-rotating within the *ac*-plane, whereas in the B_{1u} mode, the WS_2 layers expand out-of-plane and out-of-phase (Figure 3c,f). As a result, the interlayer distance does not strongly affect these motions. This analysis clearly shows why the A_{1g} vibrational mode is most sensitive to reduced interlayer distances. It also reveals why this displacement is a likely driver of the WS_2 nanotube breakdown mechanism. We anticipate that this type of breathing mode will also be important in other nanotubes formed from layered materials, such as MoS_2 or the newly discovered misfit layered compounds,[56] under compression.

Breakdown Mechanism and Comparison to Theory. Theoretical modeling of the tubes under uniaxial pressure (perpendicular to the tube axis) gives insight into the breakdown mechanism.[22] The tube layers are predicted to distort under pressure, with the innermost layer being the most affected. The layers eventually fracture at a pinching point, and the crack propagates from the inside to the outermost layer forming two-dimensional sheets.[22] Shockwave experiments reveal a similar mechanism in WS_2 nanoparticles, except the fracture propagates from the outermost layer inward.[9,23,57] These findings dovetail with our experimental results, which provide direct microscopic evidence for this mechanism. The large pressure-induced frequency shift of the A_{1g} mode suggests a strong interlayer component to the breakdown pathway. In fact, transmission electron microscope images of tubes after compression (Figure 4) display a remarkable set of fractures

DOI: 10.1021/acs.nanolett.5b03996
Nano Lett. 2016, 16, 993–999

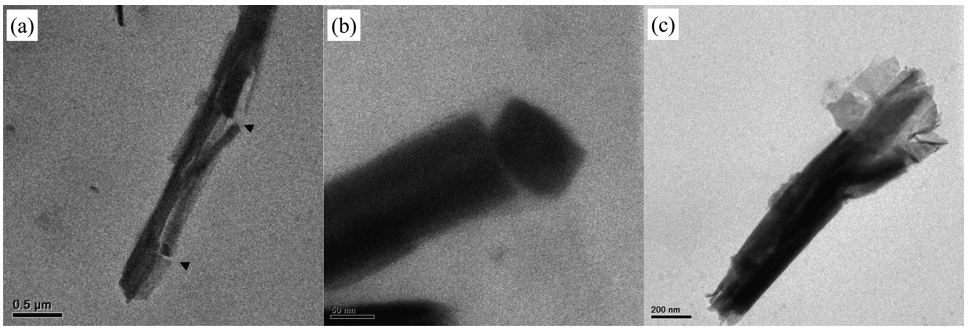

Figure 4. TEM images of the nanotubes after compression to 20 GPa in the diamond anvil cell and subsequent release, demonstrating the fractures perpendicular to the tube direction (a,b) and exfoliation of the outer layer (c).

perpendicular to the tube direction, i.e., along the direction of the A_{1g} displacement. The fractures appear to propagate from the outside inward, as evidenced by the exfoliation of the outer layer in some instances (Figure 4c). It is important to realize that this type of fracture event is fairly local, probably occurring over a range of pressures and leaving much of the nanotube unperturbed. If the entire length of the tube were to be damaged at once there would instead be a sharp discontinuity in the frequency versus pressure trends.

Although isotropic (three-dimensional) pressure is applied in our work, it is comparable to strain in that it modifies bond lengths and angles. Density functional theory calculations predict that the Raman signatures of the in- and out-of-plane modes depend linearly on axial strain.[58] Our data show that the Raman mode frequencies do indeed change linearly with pressure. The E_{2g} mode is, however, predicted to be more sensitive to tensile strain than the A_{1g} mode,[58] different than the experimental high pressure response in Figure 2. This discrepancy probably originates from the tensile strain being applied only along the length of the nanotube in the calculations, i.e., along the *a* axis, therefore not affecting the interlayer spacing as strongly as the isotropic pressure applied in our work. These differences clearly merit future investigation.[59−61]

Electronic Properties of Multiwall WS_2 Tubes under Pressure. The electronic properties of transition metal dichalcogenides are also attracting sustained attention. For instance, MoS_2 metallizes under pressure in both bulk powder and single crystal form.[40,62] Moreover, simulations of WS_2 nanotubes under tensile strain predict band gap closure above 16% nanotube elongation.[58,63] Pressure is clearly a very effective tuning parameter. We are therefore very interested in any signature or tendency toward novel electronic behavior in the tubes.

In addition to the vibrational modes discussed in prior sections, the infrared response of the WS_2 tubes displays a broad and rising electronic background under pressure that can be seen both in the absolute absorption and the absorption difference spectra (Figure 5a,b).[64] This localized absorption may be indicative of percolation. We therefore consider what can be learned from effective medium theories.[65,66] While percolation theory usually refers to the concentration of a conducting material in a nonconducting matrix (like metal nanoparticles in glass),[67] the analogy can be made to a fixed concentration in a decreasing volume. As pressure is applied, the nanotubes are forced closer together until they eventually touch (inset, Figure 5c). When enough tubes are in contact, a conductive pathway can be created, so we can think of these experiments as "sweeping concentration".

To quantify this trend, we tracked the absorption difference at 295 cm^{-1} versus pressure (Figure 5c). In line with percolation modeling of layered networks of semiconducting carbon nanotubes,[68,69] we fit the absorption difference at 295 cm^{-1} to the sigmoidal Boltzmann equation, $I = A_1 - A_2/[1 + \exp(P - P_0)/\Delta P] + A_2$, where I is the percolation probability, A_1 is the percolation at ambient pressure, A_2 is the high pressure percolation limit, P is pressure, and P_0 and ΔP are the pressure at the midpoint of percolation and pressure range from zero to full percolation, respectively. We find the percolation threshold to be P_0 = 9.3 GPa and predict that percolation will saturate at 40 GPa.[70] Our modeling also indicates that there is some percolation even at ambient conditions, demonstrating that while the individual WS_2 tubes may be relatively conducting, the ensemble properties are dominated by hopping from tube to tube. This finding is consistent with both theoretical and experimental conductivities and band gaps.[30,39,71−73] Using the position of the broad electronic background as a measure of the hopping barrier (Figure 5b), we find an activation energy of approximately 350 cm^{-1} (43 meV). Although we measured up to 20 GPa, which is close to the 19 GPa metallic transition in multilayered MoS_2,[40,62] there is no evidence for a Drude response in the multiwall WS_2 nanotubes. No metallic behavior was observed in bulk WS_2 up to 52 GPa either,[43] suggesting critical differences between the Mo and W systems that give additional stability to WS_2 and cause the analogous transition to move to much higher pressures.[43]

To summarize, we investigated the synchrotron-based infrared and Raman response of multiwall WS_2 nanotubes under pressure and compared our findings with a complementary symmetry analysis and lattice dynamics calculations. Strikingly, the A_{1g} Raman-active mode hardens at a rate that is twice that of the other vibrations. This is because the A_{1g} mode involves WS_2 slabs expanding against each other, and decreased interlayer distances naturally and preferentially constrict this motion. Transmission electron microscope images taken after compression support the possible involvement of this mode in the tube breakdown mechanism. At the same time, the high pressure infrared measurements provide unexpected insight into the electronic properties of the multiwall WS_2 tubes. Percolation is evidenced from the development of a localized absorption under compression, revealing that an ensemble of nanotubes displays macroscopic conductivity above the percolation limit. We estimate an activation energy for hopping between tubes of approximately 350 cm^{-1}.

DOI: 10.1021/acs.nanolett.5b03996
Nano Lett. 2016, 16, 993−999

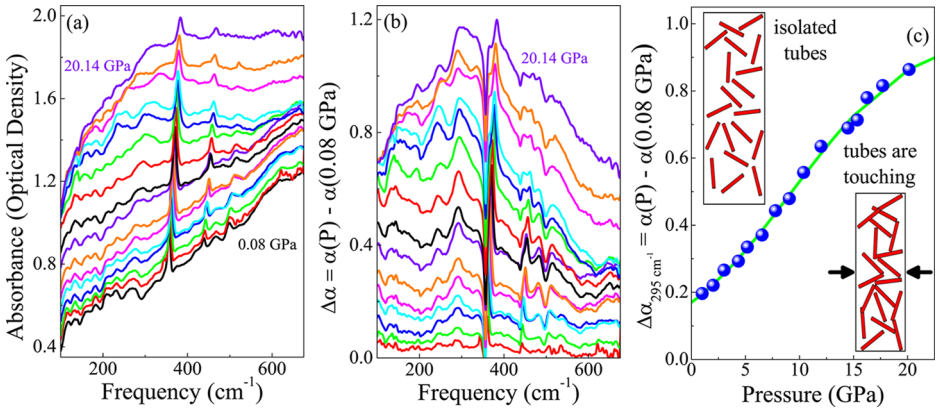

Figure 5. (a) Infrared spectra at increasing pressures. (b) Absorption difference, $\Delta\alpha = \alpha(P) - \alpha(0.08\ GPa)$, showing the increasing background due to improved conductivity under pressure caused by percolation effects. (c) Absorption difference at 295 cm^{-1} versus pressure. The green line is a fit to the percolation model described in the text. Insets: schematic views of the diamond anvil cell at low and high pressure showing the conductive pathway that forms as the tubes begin to touch.

Materials and Methods. The WS_2 nanotubes used in this study were synthesized by a bottom-up solid−gas reaction, for which a detailed growth mechanism was reported previously.[25] Briefly, tungsten oxide nanoparticles of ≈100 nm in diameter were used as a precursor to react with hydrogen (H_2) and hydrogen sulfide (H_2S) gases at an elevated temperature of 750−840 °C. The reaction consists of two steps, both carried out in the same reaction zone and following each other in a self-controlled manner. During the first step, the suboxide whiskers of 10−20 μm in length and 20−120 nm in diameter were grown by the reaction of the precursor oxide with hydrogen. In the second step, the tungsten oxide whiskers were converted into tungsten sulfide nanotubes by an outward-inward process. The reaction with H_2/H_2S started from the whiskers surface, creating the outermost sulfide layer, and continued the sulfidization of the inner oxide by the slow diffusion mode. The reaction resulted in full oxide-to-sulfide conversion and hollow WS_2 nanotube formation. The formation of the hollow core inside the nanotubes is due to the difference in specific gravity of the oxide and sulfide phases (7.15 vs 7.5 g/cm^3, respectively). The nanotubes were characterized with scanning and transmission electron microscopy (Figures 1 and 4).

The tubes were loaded into diamond anvil cells either neat or with a pressure medium (neat for Raman, vacuum grease for far-infrared, and KBr for middle infrared) for room temperature measurements. Fluorescence of an annealed ruby ball inside the diamond anvil cell was used to measure the pressure.[74] Due to the small sample size and 500 μm diamond culets, the National Synchrotron Light Source at Brookhaven National Laboratory was used for its high brightness infrared light.[75] Infrared measurements were taken from 100 to 700 cm^{-1} with a resolution of 1 cm^{-1} for all spectra. Raman measurements were performed with a 532 nm diode-pumped solid state laser, with power below 1 mW to prevent sample degradation. Raman spectra were taken from 80 to 800 cm^{-1} with a resolution of 0.5 cm^{-1} using an 1800 line per mm grating, integrated between 60 and 120 s, and averaged three times. All measurements were carried out at 300 K, and standard peak fitting procedures were employed as appropriate.

AUTHOR INFORMATION

Corresponding Author

*E-mail: musfeldt@utk.edu.

Notes

The authors declare no competing financial interest.

ACKNOWLEDGMENTS

This work was supported by the U.S. Department of Energy (DE-FG02-01ER45885), the Petroleum Research Fund (52052-ND10), the Israel National Nano-Initiative (INNI) "A Focal Technology Area (FTA) program of the Israel Council for Higher Education", and the COST Action MP1306 Titled "Modern Tools for Spectroscopy on Advanced Materials: A European Modelling Platform." The National Synchrotron Light Source at Brookhaven National Laboratory was supported by the US Department of Energy under Contract No. DE-AC98-06CH10886. The use of U2A beamline was supported by COMPRES under NSF Cooperative Agreement EAR 11-57758 and CDAC (DE-FC03-03N00144). We thank T. Heine, T. Livneh and Q.-C. Sun for useful discussions.

REFERENCES

(1) Wilson, J.; Yoffe, A. *Adv. Phys.* **1969**, *18*, 193−335.
(2) Jariwala, D.; Sangwan, V. K.; Lauhon, L. J.; Marks, T. J.; Hersam, M. C. *ACS Nano* **2014**, *8*, 1102−1120.
(3) Khan, M. F.; Iqbal, M. W.; Iqbal, M. Z.; Shehzad, M. A.; Seo, Y.; Eom, J. *ACS Appl. Mater. Interfaces* **2014**, *6*, 21645−21651.
(4) Pumera, M.; Sofer, Z.; Ambrosi, A. *J. Mater. Chem. A* **2014**, *2*, 8981−8987.
(5) Xu, G.; Wang, J.; Yan, B.; Qi, X.-L. *Phys. Rev. B: Condens. Matter Mater. Phys.* **2014**, *90*, 100505(R).
(6) Lembke, D.; Bertolazzi, S.; Kis, A. *Acc. Chem. Res.* **2015**, *48*, 100−110.
(7) Tenne, R. *Nat. Nanotechnol.* **2006**, *1*, 103−111.
(8) Novoselov, K. S.; Geim, A. K.; Morozov, S. V.; Jiang, D.; Zhang, Y.; Dubonos, S. V.; Grigorieva, I. V.; Firsov, A. A. *Science* **2004**, *306*, 666−669.
(9) Zhu, Y. Q.; Sekine, T.; Brigatti, K. S.; Firth, S.; Tenne, R.; Rosentsveig, R.; Kroto, H. W.; Walton, D. R. M. *J. Am. Chem. Soc.* **2003**, *125*, 1329−1333.
(10) Tenne, R.; Margulis, L.; Genut, M.; Hodes, G. *Nature* **1992**, *360*, 444−446.
(11) Rapoport, L.; Bilik, Y.; Feldman, Y.; Homyonfer, M.; Cohen, S. R.; Tenne, R. *Nature* **1997**, *387*, 791−793.
(12) Rapoport, L.; Fleischer, N.; Tenne, R. *Adv. Mater.* **2003**, *15*, 651−655.
(13) Active Protection NANO materials. Lubricants. http://www.apnano.com/product/lubricant/ (accessed March 25, 2015).

DOI: 10.1021/acs.nanolett.5b03996
Nano Lett. 2016, 16, 993−999

(14) Nanotech Industrial Solutions. Products. http://nisusacorp.com/product/ (accessed March 25, 2015).
(15) Rapoport, L.; Fleischer, N.; Tenne, R. *J. Mater. Chem.* **2005**, *15*, 1782−1788.
(16) Adini, A. R.; Redlich, M.; Tenne, R. *J. Mater. Chem.* **2011**, *21*, 15121−15131.
(17) Zhang, W.; Ge, S.; Wang, Y.; Rafailovich, M.; Dhez, O.; Winesett, D.; Ade, H.; Shafi, K. V. P. M.; Ulman, A.; Popovitz-Biro, R.; Tenne, R.; Sokolov, J. *Polymer* **2003**, *44*, 2109−2115.
(18) Reddy, C. S.; Zak, A.; Zussman, E. *J. Mater. Chem.* **2011**, *21*, 16086−16093.
(19) Shneider, M.; Rapoport, L.; Moshkovich, A.; Dodiuk, H.; Kenig, S.; Tenne, R.; Zak, A. *Phys. Status Solidi A* **2013**, *210*, 2298−2306.
(20) Naffakh, M.; Díez-Pascual, A. M. *Inorganics* **2014**, *2*, 291−312.
(21) Joly-Pottuz, L.; Dassenoy, F.; Belin, M.; Vacher, B.; Martin, J. M.; Fleischer, N. *Tribol. Lett.* **2005**, *18*, 477−485.
(22) Stefanov, M.; Enyashin, A. N.; Heine, T.; Seifert, G. *J. Phys. Chem. C* **2008**, *112*, 17764−17767.
(23) Cook, J.; Rhyans, S.; Roncase, L.; Hobson, G.; Luhrs, C. *Inorganics* **2014**, *2*, 377−395.
(24) Brown, S.; Musfeldt, J. L.; Mihut, I.; Betts, J. B.; Migliori, A.; Zak, A.; Tenne, R. *Nano Lett.* **2007**, *7*, 2365−2369.
(25) Zak, A.; Sallacan-Ecker, L.; Margolin, A.; Feldman, Y.; Popovitz-Biro, R.; Albu-Yaron, A.; Genut, M.; Tenne, R. *Fullerenes, Nanotubes, Carbon Nanostruct.* **2010**, *19*, 18−26.
(26) Staiger, M.; Rafailov, P.; Gartsman, K.; Telg, H.; Krause, M.; Radovsky, G.; Zak, A.; Thomsen, C. *Phys. Rev. B: Condens. Matter Mater. Phys.* **2012**, *86*, 165423.
(27) Unalan, H. E.; et al. *IEEE Trans. Electron Devices* **2008**, *55*, 2988−3000.
(28) Sun, Q.-C.; Xu, X. S.; Vergara, L. I.; Rosentsveig, R.; Musfeldt, J. L. *Phys. Rev. B: Condens. Matter Mater. Phys.* **2009**, *79*, 205405.
(29) Radisavljevic, B.; Radenovic, A.; Brivio, J.; Giacometti, V.; Kis, A. *Nat. Nanotechnol.* **2011**, *6*, 147−150.
(30) Levi, R.; Bitton, O.; Leitus, G.; Tenne, R.; Joselevich, E. *Nano Lett.* **2013**, *13*, 3736−3741.
(31) Kreizman, R.; Schwartz, O.; Deutsch, Z.; Itzhakov, S.; Zak, A.; Cohen, S. R.; Tenne, R.; Oron, D. *Phys. Chem. Chem. Phys.* **2012**, *14*, 4271−4275.
(32) Ye, J. T.; Zhang, Y. J.; Akashi, R.; Bahramy, M. S.; Arita, R.; Iwasa, Y. *Science* **2012**, *338*, 1193−1196.
(33) Zhang, C.; Wang, S.; Yang, L.; Liu, Y.; Xu, T.; Ning, Z.; Zak, A.; Zhang, Z.; Tenne, R.; Chen, Q. *Appl. Phys. Lett.* **2012**, *100*, 243101.
(34) Sun, Q. C.; Yadgarov, L.; Rosentsveig, R.; Seifert, G.; Tenne, R.; Musfeldt, J. L. *ACS Nano* **2013**, *7*, 3506−3511.
(35) Sun, Q. C.; Mazumdar, D.; Yadgarov, L.; Rosentsveig, R.; Tenne, R.; Musfeldt, J. L. *Nano Lett.* **2013**, *13*, 2803−2808.
(36) Bruno, A.; Borriello, C.; Haque, S. A.; Minarini, C.; Di Luccio, T. *Phys. Chem. Chem. Phys.* **2014**, *16*, 17998−18003.
(37) Lorenz, T.; Ghorbani-Asl, M.; Joswig, J.-O.; Heine, T.; Seifert, G. *Nanotechnology* **2014**, *25*, 445201.
(38) Steinhoff, A.; Kim, J.-H.; Jahnke, F.; Rösner, M.; Kim, D.-S.; Lee, C.; Han, G. H.; Jeong, M. S.; Wehling, T. O.; Gies, C. *Nano Lett.* **2015**, *15*, 6841.
(39) Seifert, G.; Terrones, H.; Terrones, M.; Jungnickel, G.; Frauenheim, T. *Phys. Rev. Lett.* **2000**, *85*, 146−149.
(40) Chi, Z.-H.; Zhao, X.-M.; Zhang, H.; Goncharov, A. F.; Lobanov, S. S.; Kagayama, T.; Sakata, M.; Chen, X.-J. *Phys. Rev. Lett.* **2014**, *113*, 036802.
(41) Nayak, A. P.; Pandey, T.; Voiry, D.; Liu, J.; Moran, S. T.; Sharma, A.; Tan, C.; Chen, C.-H.; Li, L.-J.; Chhowalla, M.; Lin, J.-F.; Singh, A. K.; Akinwande, D. *Nano Lett.* **2015**, *15*, 346−353.
(42) Fan, X.; Chang, C.-H.; Zheng, W. T.; Kuo, J.-L.; Singh, D. J. *J. Phys. Chem. C* **2015**, *119*, 10189−10196.
(43) Bandaru, N.; Kumar, R. S.; Sneed, D.; Tschauner, O.; Baker, J.; Antonio, D.; Luo, S.-N.; Hartmann, T.; Zhao, Y.; Venkat, R. *J. Phys. Chem. C* **2014**, *118*, 3230−3235.
(44) Wieting, T. J.; Verble, J. L. *Phys. Rev. B* **1971**, *3*, 4286−4292.
(45) Molina-Sánchez, A.; Wirtz, L. *Phys. Rev. B: Condens. Matter Mater. Phys.* **2011**, *84*, 155413.
(46) Viršek, M.; Jesih, A.; Milošević, I.; Damnjanović, M.; Remškar, M. *Surf. Sci.* **2007**, *601*, 2868−2872.
(47) Zallen, R.; Slade, M. L.; Ward, A. T. *Phys. Rev. B* **1971**, *3*, 4257.
(48) Wieting, T. J.; Verble, J. L. *Phys. Rev. B* **1972**, *5*, 1473−1479.
(49) Verble, J. L.; Wietling, T. J.; Reed, P. R. *Solid State Commun.* **1972**, *11*, 941−944.
(50) Zallen, R. *Phys. Rev. B* **1974**, *9*, 4485.
(51) Sekine, T.; Nakashizu, T.; Toyoda, K.; Uchinokura, K.; Matsuura, E. *Solid State Commun.* **1980**, *35*, 371−373.
(52) Wildervanck, J. C.; Jellinek, F. *Z. Anorg. Allg. Chem.* **1964**, *328*, 309−318.
(53) Selvi, E.; Ma, Y.; Aksoy, R.; Ertas, A.; White, A. *J. Phys. Chem. Solids* **2006**, *67*, 2183−2186.
(54) The E_{2g} and E_{1u} modes are excellent examples of this behavior, and they track each other very well.
(55) At 20 GPa, the *a* and *c* parameters for bulk WS_2 are decreased from their ambient values by 3% and 10%, respectively,[43] leading to a unit cell volume of ≈88 Å^3.
(56) Panchakarla, L. S.; Radovsky, G.; Houben, L.; Popovitz-Biro, R.; Dunin-Borkowski, R. E.; Tenne, R. *J. Phys. Chem. Lett.* **2014**, *5*, 3724−3736.
(57) Zhu, Y. Q.; Sekine, T.; Li, Y. H.; Wang, W. X.; Fay, M. W.; Edwards, H.; Brown, P. D.; Fleischer, N.; Tenne, R. *Adv. Mater.* **2005**, *17*, 1500−1503.
(58) Ghorbani-Asl, M.; Zibouche, N.; Wahiduzzaman, M.; Oliveira, A. F.; Kuc, A.; Heine, T. *Sci. Rep.* **2013**, *3*, 2961.
(59) Interestingly, the strong hardening of the A_{1g} mode and its possible contribution to the breakdown mechanism also present ways to block the tube breakdown. One strategy might be to fill the nanotubes, for example with fullerenes, providing structural support and preventing the tube walls from distorting. Nanotubes could also be natively filled by an oxide core if the synthesis is not fully completed.[76] Another option is to adopt a nanoscroll geometry,[56] for which compression might result in a tighter scroll curling instead of an overall shape distortion.
(60) The synthesis starts from formation of oxide whiskers which, in the later steps of the reaction, convert to WS_2 nanotubes by sulfidization from the outside in, thus some oxide could easily be rested in the core.
(61) We point out that the uniqueness of the A_{1g} mode may also explain nanotube cutting under intense ultrasonic treatment.[76,77] Presumably, the compression wave obtained from the collapse of a nearby droplet exerts force on the tube. As the most pressure sensitive displacement, the A_{1g} mode again forms a pinching point. If the force is strong enough, the tube cleaves into different segments, with little damage.[76,77] Strong evidence for this connection is shown in Figure 4b, where compression up to 20 GPa has driven a cleavage similar to that seen under ultrasonic treatment.[76,77]
(62) Nayak, A. P.; Bhattacharyya, S.; Zhu, J.; Liu, J.; Wu, X.; Pandey, T.; Jin, C.; Singh, A. K.; Akinwande, D.; Lin, J.-F. *Nat. Commun.* **2014**, *5*, 3731.
(63) Zibouche, N.; Kuc, A.; Musfeldt, J.; Heine, T. *Ann. Phys.* **2014**, *526*, 395−401.
(64) We note that for these measurements, the presence of a pressure medium ensures that the applied pressure is quasi-static.
(65) Choy, T. C. *Effective Medium Theory: Principles and Applications; International series of monographs on physics*; Clarendon Press, 1999.
(66) We can easily rule out several other more common assignments. There is, for instance, no evidence that the localized absorption is due to band gap closure and metallization. Such a feature should shift from the visible through the near-infrared into the middle infrared to the far-infrared before heading toward zero frequency. We find no evidence for such an effect. The development of the far-infrared localized absorption is instead quite different. It becomes more prominent under compression but does not change position. Simple ligand-to-metal (or metal-to-ligand) charge transfer excitations can be ruled out for similar reasons. A pressure−induced increase in the number of

DOI: 10.1021/acs.nanolett.5b03996
Nano Lett. 2016, 16, 993−999

point defects can, however, be detected in the infrared response and should be expected to scale as the number of defects. In our experience, these spectral features are narrow and of low intensity,[78] not strong and broad as observed in the high pressure spectrum of the WS_2 nanotubes. We therefore eliminate this assignment from consideration.

(67) Carr, G. L.; Perkowitz, S.; Tanner, D. B. *Int. J. Infrared Millimeter Waves* **1985**, *13*, 171−263.

(68) We employ a two-dimensional percolation model because the applied pressure essentially compresses the nanotubes into a thin film.

(69) Jang, H.-K.; Jin, J. E.; Choi, J. H.; Kang, P.-S.; Kim, D.-H.; Kim, G. T. *Phys. Chem. Chem. Phys.* **2015**, *17*, 6874−6880.

(70) These values differ slightly depending on the exact amount of nanotubes loaded into the diamond anvil cell.

(71) Zibouche, N.; Kuc, A.; Heine, T. *Eur. Phys. J. B* **2012**, *85*, 49.

(72) Frey, G. L.; Tenne, R.; Matthews, M. J.; Dresselhaus, M. S.; Dresselhaus, G. *J. Mater. Res.* **1998**, *13*, 2412−2417.

(73) Scheffer, L.; Rosentzveig, R.; Margolin, A.; Popovitz-Biro, R.; Seifert, G.; Cohen, S. R.; Tenne, R. *Phys. Chem. Chem. Phys.* **2002**, *4*, 2095−2098.

(74) Mao, H. K.; Bell, P. M.; Shaner, J. W.; Steinberg, D. J. *J. Appl. Phys.* **1978**, *49*, 3276−3283.

(75) Carr, G. L.; Martin, M. C.; McKinney, W. R.; Jordan, K.; Neil, G. R.; Williams, G. P. *Nature* **2002**, *420*, 153−156.

(76) Zak, A.; Ecker, L. S.; Efrati, R.; Drangai, L.; Fleischer, N.; Tenne, R. *Sensors and Transducers* **2011**, *12*, 1−10.

(77) Zohar, E.; Baruch, S.; Shneider, M.; Dodiuk, H.; Kenig, S.; Tenne, R.; Wagner, H. D. *J. Adhes. Sci. Technol.* **2011**, *25*, 1603−1617.

(78) Long, V. C.; Musfeldt, J. L.; Kamarás, K.; Adams, G. B.; Page, J. B.; Iwasa, Y.; Mayo, W. E. *Phys. Rev. B: Condens. Matter Mater. Phys.* **2000**, *61*, 13191.

DOI: 10.1021/acs.nanolett.5b03996
Nano Lett. 2016, 16, 993−999